39th AIAA/ASME/SAE/ASEE Joint Propulsion Conference and Exhibit
20-23 July 2003, Huntsville, Alabama

AIAA 2003-4941

Finite Rate Chemistry Modeling for Pollutant Emission Prediction near Lean Blow Out

G. Eggenspieler and S. Menon,
School of Aerospace Engineering
Georgia Institute of Technology
Atlanta, Georgia 30332

39th AIAA/ASME/SAE/ASEE Joint Propulsion Conference and Exhibit
July 21–23, 2003 / Huntsville, AL

Finite Rate Chemistry Modeling for Pollutant Emission Prediction near Lean Blow Out

G. Eggenspieler* and S. Menon†
School of Aerospace Engineering
Georgia Institute of Technology
Atlanta, Georgia 30332

Large Eddy Simulation (LES) of turbulent premixed combustion for operating conditions close to Lean Blow Out (LBO) in a gas turbine engine has been performed. The main objective of the study is to simulate and analyze the combustion processes and to predict the sudden exponential increase in CO emission as the equivalence ratio is decreased below a critical value. It is found that the only process that can explain the CO emission trend is the release of unburnt methane (UHC) occurring at the flame front when it locally quenches. In addition, the computed turbulent premixed combustion regime does not fall into the domain of validity of the classical G-equation approach, and, the G-equation technique can neither predict nor simulate quenching and re-ignition process. On the other hand, an alternate method based on the Linear Eddy Model (LEM) is able to simulate the combustion and turbulence interactions even in this very lean limit.

1 Introduction

Recent more stringent emission regulations have pushed for the development of more fuel efficient and low-NO_x gas turbine systems. However, design studies of new devices will require accurate prediction of emissions (CO, NO and UHC) as a function of the operating conditions. Recent measurements in a full-scale combustor (denoted DOE-HAT, hereafter)[1] showed that, as the equivalence ratio is decreased, the CO emission first decreases and then, suddenly increases exponentially. This phenomenon (which is also observed in many other liquid- and gaseous-fueled gas turbine combustors) can (in some cases) be followed by, or related, to combustion instability during which the flame undergoes rapid oscillations and eventual blows out. This process is often called the lean-blow out (LBO) and understanding and predicting this phenomenon is a major research issue.

The present effort focus on the development of a general purpose combustion model. In very lean systems, all types of premixed combustion regimes (corrugated flamelet, thin reaction zone and broken reaction zone) are encountered. Many approaches have been developed in the past. In the G-equation approach, chemistry information reside in the laminar flame speed and the turbulence enhances the flame propagation. A technique, the Linear Eddy Model (LEM) demonstrated2s here directly *reproduces* the subgrid turbulence influence upon the chemical processes. Hence we discuss the applicability of these two models in lean combustion systems.

In the present application of of interest, local flame quenching is expected. Lean premixed flame front have a low tolerance toward high turbulence and the process of flame extinction due to aerodynamic stretch can not be neglected. Combustion instabilities can also lead to flame extinction, and must therefore, be predicted. Results will show the limitation of the widely used G-equation approach and the advantages of the Linear Eddy Model.

The first part of this paper will present the G-Equation and the LEM techniques. The models used for pollutants formation are then described in some details. Combustion regimes are analyzed and the limitation of the G-equation approach is highlighted. The capability of LEM to predict flame quenching is discussed and pollutants emission predictions are discussed.

2 Numerical Formulation

The governing equations of motion for an unsteady, compressible, reacting, multi-species fluid are the Navier-Stokes equations describing the conservation of mass, momentum, total energy and N-species. In the LES methodology, the large scale motion is fully resolved on the computational grid using a time- and space-accurate scheme and only the small scales are modeled. The separation between the large (resolved) and the small (unresolved) scales is determined by the grid size ($\overline{\Delta}$). A Favre spatial top-hat filter (which is appropriate for the finite-volume scheme employed here) is employed to derive the LES equations.[2] The filtered Navier Stokes equations, and their closure will not be described here but information can be found elsewhere.[3]

*Student AIAA Member
†Professor, AIAA Associate Fellow

2.1 G-Equation

In the treatment of premixed combustion, numerous studies[4,5] use the G-equation approach due to its ability to resolve the flame behavior in the corrugated flamelet, as well as in the thin reaction zone regime, and due to its low computation cost. In this approach, the flame front is represented as a infinitely thin surface that is convected by the flow and also propagates normal to itself at a characteristic flame speed S_L, S_L being the laminar flame speed of the premixed mixture. This flame propagation speed contains the effect of the entire thermo-chemical state of the fuel-air mixture. Thus, S_L is uniquely defined for a given equivalence ratio, inlet temperature and pressure. The governing equation for the G-equation model is:

$$\frac{\partial \rho G}{\partial t} + \frac{\partial}{\partial x_i}\Big(\rho u_i G\Big) = -\rho S_L |\nabla G| \qquad (1)$$

Here, G is a progress variable that has no physical meaning except that the flame is represented as a level surface that resides between $G = 1$ (premixed fuel) and $G = 0$ (burnt products).

Applying the LES filtering on this equation leads to:

$$\frac{\partial \overline{\rho}\widetilde{G}}{\partial t} + \frac{\partial}{\partial x_i}\Big(\overline{\rho}\widetilde{u_i}\widetilde{G}\Big) = -\frac{\partial}{\partial x_i}\overline{\rho}\Big(\widetilde{u_i G} - \widetilde{u_i}\widetilde{G}\Big) - \overline{\rho S_L |\nabla G|} \qquad (2)$$

Eqn. (2) needs to be closed. The subgrid convection term is modeled using a gradient assumption that incorporates the effect of the curvature of the flame:[6] $\frac{\partial}{\partial x_i}\Big(\widetilde{u_i G} - \widetilde{u_i}\widetilde{G}\Big) = \overline{\rho} D_T \widetilde{\kappa} |\nabla \widetilde{G}|$ where $\widetilde{\kappa}$ is the flame curvature defined as $\widetilde{\kappa} = \nabla \mathbf{n} = \nabla(-\nabla\widetilde{G}/|\nabla\widetilde{G}|)$, ($\mathbf{n}$ is the unit normal vector oriented in the direction of flame propagation). The flame front propagation term $\overline{\rho S_L |\nabla G|}$ is modeled as $\overline{\rho} S_F |\nabla \widetilde{G}|$ where S_F is the flame speed propagation. S_F depends upon the combustion regime and has to be modeled. For laminar flow, $S_F = S_L$ and for turbulent flows $S_F = S_T$. In this study, the model developed by Pocheau[7] is used, $S_T = S_L(1 + 20.0(u'/S_L)^2)^{0.5}$.

In contrast to the original "laminar" interpretation of the G approach where the flame is considered as an infinitely thin interface between $G = 0$ and $G = 1$, the LES-resolved variable $\widetilde{G}$ can range from 0 to 1. Value of $\widetilde{G}$ between 0 and 1 represents a measure of the flame brush thickness defined as the average location of the instantaneous thin flames during an integration time step. However, the heat release is included in this formulation over a thin zone using a heat of formation approach.

2.2 LEM Methodology

The idea behind Linear Eddy Model (LEM) is to separate large scale advection and subgrid processes separately but concurrently. Scalars (energy and species mass fraction) will be tracked by a Lagrangian technique while the conservation of mass and momentum is solved using the classical Eulerian approach. To describe this technique more precisely, consider the governing equation of a scalar ψ

$$\frac{\partial(\rho\psi)}{\partial t} + \frac{\partial(\rho\psi u_i)}{\partial x_i} + \frac{\partial}{\partial x_i}\Big[-\rho D_\psi \frac{\partial \psi}{\partial x_i}\Big] = \rho \dot{w}_\psi \qquad (3)$$

where D_ψ is the molecular diffusion coefficient and $\dot{w}_\psi$ is the chemical source term. By splitting u_i using LES techniques ($u_i = \widetilde{u_i} + u_i'$) a set of two equations is obtained.

$$[\overline{\rho}\widetilde{\psi}](t + \Delta T) - [\overline{\rho}\widetilde{\psi}](t) = \frac{1}{n_{in}}\sum_{i=1}^{n_{in}} \overline{\rho}\psi^* - \frac{1}{n_{out}}\sum_{i=1}^{n_{out}} \overline{\rho}\psi^* \qquad (4)$$

$$\frac{\partial(\overline{\rho}\psi^*)}{\partial t} + \frac{\partial(\overline{\rho}\psi^* u_i')}{\partial x_i} + \frac{\partial}{\partial x_i}\Big[-\rho D_\psi \frac{\partial \psi^*}{\partial x_i}\Big] = \overline{\rho}\dot{w}_{\psi^*} \qquad (5)$$

Where ψ^* is the scalar value at the LEM level and $\widetilde{\psi}$ is the arithmetic average of all ψ^* contained in a given LES cell. n_{in} and n_{out} represent the number of LEM cells respectively entering and leaving an LES cell during an integration time step ΔT. The number of LEM contained in an LES cell being constant, $n_{in} + n_{out} = 0$. n_{in} and n_{out} are determined using flux based on the resolved velocity field ($\widetilde{u_i}$). Eq. 4 describes the resolved convection while Eq. 5 describes the unresolved turbulent convection, the molecular diffusion and the chemical reaction rate. Scalar fields are resolved on a one dimensional line embedded in a LES cell. Molecular diffusion and chemical reactions are resolved at the LEM level. In this study, chemical reaction rates are computed using a 5-species 1-step mechanism. Subgrid turbulence convection is simulated by rearranging the scalar field on the LEM line. This rearrangement (or stirring) mimics the action of an eddy of size l upon the scaler field. The location of this event is chosen from a uniform distribution, the frequency of stirring per unit length (λ) is derived from 3D scaling laws as:

$$\lambda = \frac{54}{5}\frac{\nu Re_{\overline{\Delta}}}{C_\lambda \overline{\Delta}^3}\frac{[(\overline{\Delta}/\eta)^{5/3} - 1]}{[1 - (\eta/\overline{\Delta})^{4/3}]} \qquad (6)$$

C_λ represent the scalar turbulent diffusivity and is determined as 0.067. The eddy size (l) is chosen from the following PDF:

$$f(l) = \frac{(5/3)l^{-8/3}}{\eta^{-5/3} - \overline{\Delta}^{-5/3}} \qquad (7)$$

where $\eta = N_\eta \overline{\Delta} Re_{\overline{\Delta}}^{-4/3}$. The empirical constant N_η reduces the effective range of scale between the integral length scale and η but does not change the turbulent diffusivity ($N_\eta \in [1.3; 10.78]$).

2.3 ISAT and Artificial Neural Network (ANN) Structure

Chemical reaction rates computation via direct integration of the system of Ordinary Differential Equations (ODE) has a high computation cost even when a 5 species, 1 step mechanism is considered. The cost becomes prohibitive once a more accurate chemical mechanism is concerned. Computational cost can be reduced using an *InSitu* Adaptive Tabulation (ISAT) method[8] in an efficient manner[9] (Speed-up of 30 were reported[10]). In the ISAT method, only the accessed chemical composition is stored in a database. When the same composition and temperature re-occurs, the reaction rates and final temperature are retrieved from the database rather than recomputed. The retrieve algorithm determines the efficiency of the ISAT method. Nevertheless, the memory cost of ISAT in LES can be significant since the ISAT table continues to grow over multiple flow through times and can eventually overflow the memory.

An ANN structure, by definition, is a structure of several interconnected nonlinear elements, which functions like biological neurons with an ability to learn from a set of input-output parameter space it is subjected to, and then, predict the output for a new sample set with a sufficient level of accuracy.[11] The information in a network is stored in the form of weights and biases (or neurons), which are computed iteratively in the learning phase of the network training.

The inherent ability of ANN to model highly complex nonlinear processes makes it a suitable choice to model nonlinear behaviors of temperature and species concentrations in a chemical reaction. There are several training and learning algorithms present in literature. In general, a perceptron learning rule is favored for our applications, since it is generally robust in its ability to generalize from its training vectors and learn from initially randomly distributed connections.[12]

Mathematically, the output for a multi-layer perceptron (MLP) network can be represented as :

$$Y_i^L = F\left(\sum_{j=1}^{n_L} w_{ij}^L O_j^{L-1} + \beta_i^L\right) \quad for \quad i = 1, ..., n_L \quad (8)$$

where Y_i^L is the output of the ith neuron of the Lth layer, w_{ij}^L represents the weight value for the connecting jth neuron of the (L-1)th layer and the ith neuron of the Lth layer, β_i^L is the bias value, n_L is the total number of neurons in the Lth layer, and F is the transfer function. Hyperbolic-tangent function is used as the transfer function most commonly. Figure 1 shows the typical layout of a three layer neural network, that has been used significantly in the current work.

The major advantage of an ANN structure is in terms of the tremendous reductions in CPU times (as opposed to direct integration methods) and disk storage (as opposed to the conventional search/retrieve ISAT algorithms). The choice of the correct ANN variables and structure, however, is a critical factor that defines the efficiency and accuracy of the resulting ANN.

2.4 Pollutant Models

In the present study, we are primarily interested in predicting CO, NO_x and UHC emission as a function of equivalence ratio. Here, UHC represents the unburnt fuel (CH_4) that is released in the burnt product region in the event of flame quenching. The production of these pollutants occur due to a combined effect of chemical kinetics and turbulent fluid dynamical processes.

In the following sections, we discuss the closure of the chemical source term $\overline{\rho}\widetilde{\dot{w}}_m$ for CO, NO_x and UHC.

2.4.1 Flamelet Library

The term flamelet library refers, in all this study, to an offline chemical data base generated using CHEMKIN-PREMIX program outputs. The resolved value of a given chemical parameter ψ at the resolved scale $\widetilde{\psi}$ depends upon the resolved scale mixture fraction ($\widetilde{Z}$) as well as the level of unmixidness of the premixed mixture that is measured via the variance of the mixture fraction ($\widetilde{Z''^2}$). These two scalars are tracked during the computation and the chemical parameter ψ can be determined using an assumed PDF f (Beta PDF in this case). The PDF shape is a function of $\widetilde{Z}$ and $\widetilde{Z''^2}$. Thus $\widetilde{\psi} = \int \psi(Z) f(\widetilde{Z}, \widetilde{Z''^2}) dZ$.

For perfectly premixed combustion, $\widetilde{Z}$ is a constant and $\widetilde{Z''^2}$ is equal to zero. For partially premixed systems, the mixture fraction approach is valid only if all species molecular diffusion coefficients are equal whereas these coefficients can be different if a constant mixture fraction approach is used. This has no consequences on the G-equation study. For LEM, the 5-species chemistry uses different molecular diffusion coefficients but because the system is assumed to be perfectly premixed, the flamelet library data can still be used.

2.4.2 Carbon Monoxide (CO)

CO is formed and/or destroyed by four major mechanisms. All of these mechanisms have to be properly modeled in the simulation, and therefore, are discussed in some detail. The four mechanisms (and the nomenclature used to identify them) are (i) the formation of CO at the flame front (subscript ff), (ii) the oxidation of CO in the post flame region (subscript ox), (iii) the dissociation of CO_2 (subscript dis) and (iv) the formation of CO via oxidation of unburned CH_4 (subscript $oxuhc$) The overall production/destruction rate of CO can then be written as $\widetilde{\dot{w}}_{CO} = \widetilde{\dot{w}}_{CO,ff} + \widetilde{\dot{w}}_{CO,ox} + \widetilde{\dot{w}}_{CO,dis} + \widetilde{\dot{w}}_{CO,oxuhc}$.

Due to the presence of radicals in the flame front (especially O), a large amount of CO will be produced at the flame front ($Y_{CO,ff}$). $Y_{CO,ff}$ is given by the flamelet library. The formation of CO at the flame front is treated as a jump relationship, i.e. CO production rate at the flame front is proportional to the rate of fuel consumption $\dot{w}_{fuel}$.[13,4] Thus, the CO production at the flame front is modeled as:

$$\widetilde{\dot{w}}_{CO,ff} = -\frac{\dot{w}_{fuel}}{C_{ref}} Y_{COff} \tag{9}$$

where $\dot{w}_{fuel}$=S_F | $\nabla \widetilde{G}$ | and C_{ref}=1 in the G-equation approach. In the LEM approach, $\dot{w}_{fuel}$ is taken as the arithmetic average of the fuel consumption rate of all the LEM cells contained inside an LES cell and C_{ref} is equal to the value of the mixture fraction.

Typically, the front flame formation lies, in terms of mass fraction, between 1 and 3 percent. It should be noted that the value Y_{COff} computed by CHEMKIN-PREMIX corresponds to the pollutant formation of a laminar non-stretched flame. In the flamelet assumption, the flame is wrinkled by turbulent eddies but cannot change the laminar flame structure. Therefore, turbulence has no direct effect on the pollutant emission from the local laminar flame.

The above assumption is not generally valid since flame stretch can modify the local laminar flame structure (in the thin-reaction zone regime) and this can impact the local CO formation at the flame front. However, at this time, this effect is neglected and only a more detailed chemistry mechanism can predict the exact amount of CO produced at the flame front for different combustion regimes.

Once CO is formed, it will be oxidized into CO_2. The flamelet library provides the oxidation time scale $\tau_{CO,ox}$ of CO. The rate of oxidation of CO is given as $\widetilde{\dot{w}}_{CO,ox} = -(1/\tau_{CO,ox})\widetilde{Y}_{CO}$. The oxidation time scale is based upon the product temperature at a given equivalence ratio. To account for change in temperature due to heat loss, the CO oxidation time scale is corrected as follow:

$$\frac{1}{\tau_{CO,ox}} = \frac{1}{\tau_{CO,ox}} exp\Big(E_A \frac{T - T_b}{T * T_b}\Big) \tag{10}$$

where T is the actual LES temperature, T_b is the burnt products temperature predicted by the flamelet library and E_A is the activation energy chosen by curve fitting with the flamelet library data. The reaction rate of CO oxidation in the post flame region is independent of the subgrid turbulence since CHEMKIN-PREMIX does not take into account the influence of turbulence. This assumption will be discussed later.

The equilibrium value is defined as the CO mass fraction reached when the rate of CO consumption by oxidation equals the rate of CO production via CO_2 dissociation. The flamelet library determines the CO mass fraction at equilibrium ($Y_{CO,eq}$). The rate of formation of CO via CO_2 dissociation is taken as $\widetilde{\dot{w}}_{CO,eq}$= $P_b(1/\tau_{CO,ox})Y_{CO,eq}$ where P_b=0 on the reactant side and P_b=1 on the product side.

The earlier numerical study[14] claimed that UHC were not responsible for CO emission. Improvement in the computation and generation of the library shows that the influence of UHC has to be taken into account. It will be demonstrated later in section 6.2 that combustion takes place in the broken reaction zone regime. Therefore, UHC release via flame quenching in very lean system is expected and its re-ignition will be a key parameter for CO emission predictions. Furthermore the level of turbulence in the flow is assumed to be high enough such that re-ignition is purely chemistry controlled and occurs at a rate defined in other study.[15] Once ignited, the unburnt CH_4 is assumed to be entirely oxidized into CO.[4] This assumption is questionable and can lead to substantial errors in the predictions.

2.4.3 Oxides of Nitrogen (NO_x)

Two mechanisms related to NO formation are taken into account in the present study. The first mechanism is the production of NO at the flame front (subscript ff) and the second one is the production of nitric monoxide due to the Zeldovich mechanism in the post flame region (subscript zel).

Prompt NO is formed at the flame front and the amount formed ($Y_{NO,ff}$) is given by the library. The rate of formation of NO at the flame front is computed as the amount of CO formed at the flame front, thus $\widetilde{\dot{w}}_{NO,ff}$ =$\dot{w}_{fuel}/C_{ref}Y_{NOff}$

The rate of formation of NO in the post flame region is computed using the Zeldovich mechanism under the quasi-steady assumption, i.e., the concentration of O and N radicals are assumed equal to the O and N equilibrium concentrations. The Zeldovich mechanism is described in many books.[16] Under the quasi-steady assumption, where O, N, N_2 and O_2 mass fraction are considered to be constant. Nevertheless, the reaction $N_2 + O_2 \rightleftharpoons 2NO$ is assumed to be out of equilibrium, and thus, NO is formed at a constant rate and is extracted from the chemistry data base.

2.4.4 Unburnt Hydrocarbons (UHC)

If the flame front is partially quenched (mainly due to aerodynamic stretch), pockets of unburnt methane, or UHC, will be released in the post flame region. UHC will oxidize at a rate governed by an Arrhenius-law.

In order to predict UHC production at the flame front, the Intermittent Turbulence Net Flame Stretch

Model is implemented (INFTS[17]). In this study, only UHC production via aerodynamic stretch flame quenching is modeled.

3 The DOE-HAT Geometry

The geometry of the DOE-HAT combustor is shown in Fig. 2 (a). In this combustor, the premixed mixture enters the combustor in a swirling manner through a circular slot. The flame is stabilized by the recirculation in the base of the dump and also by the recirculation created by the center body. Figure 2 (b) shows the characteristic grid distribution. A high accuracy interpolation scheme is used to transfer information from/to the centerline cartesian domain to/from the cylindrical grid (see bottom left hand side corner of Fig. 2 (b)).

The length of the combustion chamber is 0.5 m, its radius is 0.053 m and the inlet is located between 0.0173 m and 0.0314 m from the centerline. The length of the combustor is chosen so that the emissions predictions (which is only available at 0.381 m from the dump plane) can be computed and compared with data.

The inflow characteristics are chosen as given in the earlier DOE-HAT experiment: the fuel is methane (CH_4) and the reactants enter the combustor with a temperature of 700 K, a pressure of 1.378 MPa., and a mean inflow velocity of 68.6 m/s. The flow is swirling and the swirl number is 0.6. The Reynolds number based on the inlet velocity and the diameter of the center-body is 230,000. A random turbulent field is added to the inflow mean velocity and a subgrid turbulence intensity of around 7 percent is used to specify the incoming subgrid kinetic energy. Characteristic based inflow and outflow boundary conditions[18] are employed for all the reported simulations.

4 Combustion Dynamic

Lean combustion systems are particularly sensitive to small perturbations in heat release that can lead to flame extinction. The instabilities are known to grow as the operating equivalence ratio is decreased (larger sensitivity of the flame as S_L decreases). Nevertheless, the increase in heat release (as Φ increases) can also increase the instabilities. In this DOE-HAT combustor, the oscillations limit cycle is always reached (i.e., the amplitude of the oscillations is constant in time). The heat release ratio ($T_{products}/T_{reactants}$), the laminar flame speed (S_L) and the relative r.m.s. pressure oscillation (P_{RMS}=$\sqrt{\overline{(P-\overline{P})^2}}/\overline{P}$) are shown on Table 1.

Results show that the decrease in laminar flame speed is the factor explaining the increase in pressure oscillations as the equivalence ratio is decreased. These instabilities can promote flame extinction.

Φ	$\frac{T_{products}}{T_{reactants}}$	S_L (cm/s)	P_{RMS} percent
0.41	2.34	6.9	2.3
0.53	2.65	19.5	1.33

Table 1 Heat release ratio, laminar flame speed and pressure oscillations for two different Φ.

5 Pollutants Emission

5.1 CO Emission

A wide variety of mechanisms have to be taken into account to explain the trends and the value of CO emission in a specific combustion chamber. This study concentrates on the following mechanisms (the following list is, of course, non-exhaustive):

- Lack of oxidation of CO formed at the flame front.
- UHC formation via local flame quenching, oxidation in CO in the post flame region and sensibility of the prediction with regard to UHC oxidation rate.
- Influence of the flame speed model.
- Reduction in CO oxidation rate due to heat losses at the combustion chamber walls.
- Influence of the level of unmixindness in the inflow reactant mixture.
- Influence of the turbulence on the oxidation processes in the post flame region.

5.1.1 No UHC are considered

The entire amount of CO formed at the flame front is oxidized before reaching the emission probe. To ensure the correctness of the oxidation rate computation, the values given by the flamelet library are compared to values obtained when the CO oxidation rate is directly computed assuming an Arrhenius law. The CO oxidation reaction is: $CO + OH \leftrightarrow CO_2 + H$ and the CO oxidation rate is expressed as:

$$\frac{d[CO]}{dt} = -k_i[OH]_e\Big(1+\frac{[CO]_e}{[CO_2]_e}\Big)([CO]-[CO]_e) \quad (11)$$

where the reaction rate k_i is given by an Arrhenius law k_i=$4400.0T^{1.5}exp(-373/T))$ (units are kmol, m, K and sec). The comparison for different equivalence ratio is given in Table 2.

Values reported in Table 2 are relatively close, thus confirming the correctness of library calculations. Furthermore, Eq. 11 predicts an even higher CO oxidation rate for Φ<0.5, thus verifying the conclusion that the CO formed at the flame front is not responsible for the "knee" in the CO emission curve.

Φ	$1/\tau_{CO,ox}$ (Eq. 11)	$1/\tau_{CO,ox}$ (Library)
0.41	2089	1523
0.43	2853	2215
0.45	3826	3375
0.47	5045	4571
0.49	6539	6426
0.51	8402	8912
0.53	10589	11021

Table 2 Comparison of the CO oxidation computed by the library and by Eq. 11.

5.1.2 Influence of the Turbulent Flame Speed Model.

The turbulent flame speed model can affect pollutant emission prediction because it determines the flame length. The longer the flame, th shorter the residence time of CO formed at the flame front. The model developed by Pocheau is used in this study. $S_T{=}S_L(1+\beta(u'/S_L)^2)^{0.5}$. In order to match experimental data, β is generally taken to be 20.0. An upper limit (ζ is set for u'/S_L). A decrease in β and/or ζ correspond to a decrease in turbulent flame speed. Here, we tested different values of β and ζ are summarized in Table 3

Case	β	ζ	Y_{CO}
1	20.0	16.56	0.97
2	10.0	10.00	3.7
3	7.0	10.00	34.1

Table 3 Constants used in the turbulent flame speed model and the related CO emission.

CO mass fraction as a function of the distance from the dump plane are shown on Fig. **??**. As the turbulent flame speed decreases, the flame length and the flame thickness increases. This is clearly show on Fig. **??** by the shift of the maximum CO mass fraction. This maximum shift farther from the dump plane as a direct consequence of the increase in flame length. Unfortunately, for the best of these results (β=7.0 and ζ=10.0), the G-field (i.e. the flame) lost its structures: convection effects are larger than flame propagation, and the flame thickness is very large (of the order of some centimeters). The characteristic of premixed flamelet combustion is not valid anymore.

5.1.3 Flame Quenching and UHC

Following the conclusions of other studies,[4] UHC is considered as a second source of CO. UHC is oxidized in the post-flame region forming CO later in the combustion process. The time required for UHC oxidation shortens the total CO residence time before reaching the emission probe. Thus, one expects that a certain amount of CO present in the post-flame region will not reach equilibrium before passing at the location of the emission probe. The UHC oxidation rate in CO is computed as:

$$\frac{d[UHC]}{dt} = -[UHC][O_2]Aexp\Big(-\frac{E}{T}\Big) \qquad (12)$$

Two models are considered. Table 4 shows the emission results.

Model	A	E	Y_{CO}
High oxidation rate[4]	$6.25*10^{16}$	23000	0.97
Low oxidation rate[15]	$2.4*10^{16}$	26100	8.1

Table 4 Comparison of CO emission at the location of the emission probe for different UHC oxidation model for Φ=0.41. CO mass fractions are given in ppm @ 15 percent excess O_2. 0.97 corresponds to the value of CO mass fraction at equilibrium. For Φ=0.41 the ratio between both oxidation rate (for a given [UHC]) is 1.77

If the UHC oxidation rate is too fast, the CO residence time in the post-flame region is large enough to ensure complete CO oxidation while a lower UHC oxidation rate release CO later in the combustion process and a certain amount of this CO will not reach equilibrium before reaching the emission probe. This phenomena is an explanation for the trend in the CO emission curve.

For low equivalence ratio (Φ<0.5), 2 to 4 percent of the flame is predicted to quench. Fig. 4 shows the flame surface and CO and UHC mass fraction. The CO mass fraction isolines follow UHC mass fraction isolines, thus demonstrating that UHC is not a negligible source of CO. This is confirmed in Fig. 5. A large portion of CO formed via UHC oxidation is oxidized early in the post-flame region (X<0.1 m in Fig. 5). But the amount of CO released later in the combustion process (X>0.15 m in Fig. 5) is large enough such that the entire amount of CO can not be oxidized before reaching the location of the emission probe.

5.1.4 Heat Losses

The experimental combustion chamber walls are water cooled, whereas, the numerical setup consider the walls as being adiabatic. Because heat losses may reduce CO and UHC oxidation rates a heat loss model is implemented. The cooling water temperature (T_w) is assumed to be 300K while the wall thickness (δ_w) is assumed to be 1 inch (2.54 cm). This is presented on Fig. 6.

The temperature of the boundary grid point (T_{GC}) is a function of the computed LES temperature (T_{LES}) and the distance from the wall to the computed LES grid point (dY). T_{GC} is given by:

$$T_{GC} = \Big(\frac{T_{LES}-T_w}{\delta_w+dY}\Big)(\delta_w - dY) + T_w \qquad (13)$$

Results do not exhibit any change in the CO profile at the emission probe location. The CO oxidation rate

is lower in the thermal boundary layer due to the decrease in region close to the combustion chamber walls. At the same time the residence time increases in the momentum boundary layer. The CO oxidation rate decreases in the boundary layer region is balanced by the increase in residence time.

5.1.5 *Partially Premixed System*

Other studies of the same combustion chamber[19] suggests that the CO emission trend is due to the non-uniformity of the incoming mixtures. If the system is considered as being partially premixed, $\widetilde{Z}$ and $\widetilde{Z''^2}$ can not be considered as constant and zero, respectively. In a partially premixed system, the LES filtered governing equations of $\widetilde{Z}$ and $\widetilde{Z''^2}$ are:[6]

$$\frac{\partial \overline{\rho}\widetilde{Z}}{\partial t} + \frac{\partial}{\partial x_i}\left(\overline{\rho}\widetilde{u_i}\widetilde{Z}\right) = \frac{\partial}{\partial x_i}\left((D + D_T)\overline{\rho}\frac{\partial \widetilde{Z}}{\partial x_i}\right) \quad (14)$$

$$\frac{\partial \overline{\rho}\widetilde{Z''^2}}{\partial t} + \frac{\partial}{\partial x_i}\left(\overline{\rho}\widetilde{u_i}\widetilde{Z''^2}\right) = \frac{\partial}{\partial x_i}\left(D_T\overline{\rho}\frac{\partial \widetilde{Z''^2}}{\partial x_i}\right) + 2\overline{\rho}D_T\left(\nabla\widetilde{Z}\right)^2 - \overline{\rho}\widetilde{\chi} \quad (15)$$

Here D is the molecular diffusivity and D_T is the subgrid turbulent diffusivity. Both D and D_T are obtained assuming a unity Lewis number, thus $D{=}\nu$ and $D_T{=}\nu_T$.

Here, an eddy turbulent diffusivity model is employed to close the convective subgrid flux. The closure for filtered scalar dissipation rate ($\widetilde{\chi}$) is an important issue. It represents the effect of subgrid turbulence on $\widetilde{Z}$ which tends to reduce the variance of mixture fraction (homogenize the mixture) and is modeled as $\widetilde{\chi}{=}2D|\widetilde{\nabla Z''}|^2$.[6] Because $|\nabla Z''|$ is an unknown quantity, $\widetilde{\chi}$ is computed as $\widetilde{\chi}{=}2\epsilon/k^{sgs}\widetilde{Z''^2}$. The dissipation of the subgrid TKE ϵ in the above expression is directly related to the subgrid kinetic energy: $\epsilon = C_\epsilon(k^{sgs})^{3/2}/\overline{\Delta}$.

The idea behind the consideration of a non-uniform inflow mixture fraction profile is the creation of relatively cold post flame region - a direct consequence of regions of low equivalence ratio - that will be characterized by a low CO oxidation rate.

Inflow equivalence ratio profile is plotted on Fig. 7 (a) and is obtained from experiments. The variation in equivalence ratio is relatively small and agrees with the assumption that the DOE-HAT combustor is operating under nearly perfectly premixed combustion. Fig. 7 (b) show the time averaged mixture fraction. Turbulent convection mixes the gases (reactants as well as products) and mixture fraction gradients decrease. At the location of the emission probe, the CO mass fraction equals its equilibrium value. Therefore, presence of very lean reactants pockets can not explain the CO emission trend.

5.1.6 *Mixing Time Scale*

In processes like CO or UHC oxidation, a turbulent mixing time scale (t_{mix}) can be introduced and a reaction time scale can be defined as the minimum between the chemical and the mixing time scale. This so-called Eddy-Break Up (EBU) model should not be used in a LES simulation because of its lack of accuracy: $t_{mix}{\propto}\Delta/u'$ only gives an order of magnitude of the mixing time scale and is grid size dependent. A very sensitive process like CO oxidation can not tolerate such lack of accuracy. Furthermore, due to the length of the combustion chamber, post flame region LES cells far from the flame are large enough so that their resolution may not fall into the inertial range, thus no mixing time scale can be defined using inertial range scaling laws. Therefore, it will be assumed that all pollutants formation and destruction rates are chemistry controlled. Computation show that, when t_{mix} can be defined, it is of the order of magnitude of the chemical time scale, thus confirming that no EBU model is required.

5.1.7 *Summary*

Heat losses can not be considered as a factor influencing CO emission and a slight non-uniformity in the inflow mixture fraction is not able to explain the trend. Only UHC production (CO source late in the post-flame region) appears to be responsible for the exponential increase of the CO emission when Φ is decreased under 0.45. This increase is proportional to the CO and UHC oxidation rates. Therefore, accurate oxidation rates are required. Furthermore, the use of a steady state quenching model (INFTS) for a time dependent LES simulation may only predict the order of magnitude of UHC production when local flame quenching occurs. The influence of subgrid turbulence as a mixing process is neglected. This assumption is questionable and should be revisited.

Final emission prediction for different equivalence ratio are presented on Fig. 8. The trend is well reproduced but the emission for very lean mixtures ($\Phi{=}0.41$) is under- predicted. As stated above, greater accuracy requires an extensive improvements in flame quenching and oxidation rates models.

In this study, if the effect of flame quenching is simulated (i.e. UHC production), flame doe not actually quench. This is due to the fact that G-equation model can not model quenching and re-ignition. The main challenge for accurate pollutants emission prediction is the ability to predict flame quenching and UHC formation. This problem requires a different approach as described later.

5.2 NO Emission

NO emission is presented in Fig. 8. NO emission prediction is in good agreement with experiments for low equivalence ratio but is under-predicted when Φ

increases. Because post-flame mechanisms are responsible of the largest portion of NO emission for Φ>0.5 (clearly shown in Figs. 10 (a) and (b)), results suggest that the NO formation rate in the post-flame region is under-predicted. Other factors, like poor macroscopic fuel unmixindness[20] can increase NO formation at the flame front and increase the overall NO emission. In this study, the incoming mixture is assumed to be perfectly premixed and this parameter is not taken into account.

6 Combustion Regimes

6.1 Combustion Regimes Diagram

The different regimes of premixed combustion depends upon two key parameters: the chemical composition of the premixed system and the turbulence intensity.

Numerous regimes diagrams for premixed combustion have been proposed.[21,22] A very useful combustion diagram for LES of turbulent premixed combustion was proposed by Pitsch.[23] The regime diagram for LES of turbulent combustion is shown of Fig. 11. Six regimes are present in this graph and the methods used to model the flame behavior are different for all these regimes.

In the corrugated flamelet and the wrinkled flamelet regime the flame thickness is smaller than the Kolmogorov scale (Ka<1). In this case, flame speed enhancement is a result of surface increase by the turbulent wrinkling. If turbulent eddies are able to penetrate the flame preheat zone but not into the reaction zone (1<Ka<100), the combustion regime is called the thin-reaction-zone regime. Flame speed enhancement is directly linked to the turbulent transport of heat and radicals into the preheat zone and the thickening of the preheat zone. Flame speed models for the corrugated flamelet regime[24] and the thin reaction zone regime[25] are available. If the turbulence level is raised even further, the Kolmogorov scale becomes smaller than the reaction zone (Ka>100) and the smallest turbulent structures have the ability to perturb the reaction process by destroying the reaction zone structure, thus promoting flame quenching.

The LES resolution is now considered. If the grid size is reduced until all length scales relatives to Eq. 1 and all fluid mechanics scales are resolved, flame propagation is said to occur in the laminar flamelet G-Equation DNS regime and $S_F = S_L$. If the grid size is decreased until the flame structure (preheat and reaction zones) is resolved, the full DNS level is reached.

6.2 Local Combustion Regimes

The Karlovitz number is computed from instantaneous data at different locations inside the combustion chamber and for different equivalence ratio. The value has a significance only where the flame front is located, therefore, Ka_F is computed, where Ka_F=Ka*H_F with H_F=1 if the fuel reaction rate is non-zero and H_F=0 otherwise. Results from flame modeled via the G-equation approach is shown on Fig. 12 (a) while Fig. 12 (b) shows the Karlovitz number computed with LEM. As expected the Karlovitz number decreases with an increase in equivalence ratio because the richer the mixture, the smaller the flame thickness. The Karlovitz number is higher at location close to the dump plane and in the shear layer created at the edges of the inflow pipe. These data are *instantaneous* snapshots of the flow field but a large number of these instantaneous data is post-processed to ensure that 12 is an accurate description of the instantaneous Karlovitz number.

For Φ=0.41 and Φ=0.45, the larger portion of the flame fall into the broken reaction zone. Because no flame speed models are available for this combustion regime, the G-equation approach is not well suited for Φ<0.45. On the other hand, no such limitation exist for LEM. Furthermore, flame is expected to locally and/or partially quench. Quenching can not be predicted by the G-equation techniques while the LEM is able to capture the phenomena leading to extinction. Unfortunately, the single step mechanism used to treat the chemistry in the LEM study can only quench if flammability limit is reached and, in general, radicals have to be incorporated into the chemical mechanism if quenching via aerodynamic stretch has to be predicted. Nevertheless, LEM can handle this if the if the chemical mechanism is detailed enough.

7 LES - LEM vs. LES - G-equation

.

7.1 Flame Characteristics

Models describing premixed combustion are generally not valid in all combustion regimes. The G equation approach is valid in all regimes except the broken reaction zone. This has been demonstrated theoretically[26] as well as numerically.[27] Furthermore, all flame speed models fail and behave differently in the limit of a high u'/S_L ratio, i.e., in the range of operation of the DOE-HAT combustion chamber for low equivalence ratio (low S_L). Table 5 summarizes the behavior of the ratio $(S_T - S_L)/S_L$ for large u'/S_L.

Flame speed Model	Behavior for large u'/S_L
Pope[6]	$\propto\sqrt{\Delta u'}$
Pocheau[7]	$\propto u'$
Smith's simulations[27]	Tends toward 0

Table 5 Behavior of different turbulent flame speed for high turbulence intensity

In Pocheau's model, an upper limit on u'/S_L is needed, such that S_T can not indefinitely increase. Smith numerical study reproduced a more accurate turbulent flame speed behavior. The time averaged

Φ	Flame length (LEM)	Flame length (LES)
0.53	3.5	1.5
0.45	6.5	3.0
0.41	7.5	3.5

Table 6 Flame length for different equivalence ratio and different combustion model. Flame length are given in cm.

turbulent flame speed computed in his study tends toward 0 as the frequency of quenching events increases.

The LEM methodology is valid in all combustion regimes and does not require any models other than the stirring frequency and eddy size PDF (models obtained from 3D inertial range turbulence scaling). In the wrinkled flame zone, no turbulent stirring event occurs in the LEM domain, thus the reaction progress locally at S_L. In the corrugated flamelet regime, stochastic rearrangement of the LEM field mimics the action of flame wrinkling by subgrid eddies. The increase of flame surface is simulated by an increase in the number of crossings between the flame surface and the LEM line. In the thin-reaction-zone, the flame transport in the preheat zone is enhanced by the frequent occurrence of stirring events at the LEM level. In the broken reaction zone, the action of stirring can break the flame structure and if the chemical mechanism includes the major radicals, stirring events have the capability to quench the flame. This versatility makes LEM a very powerful method.

Time averaged flame length for different equivalence ratio is summarized in Table 6.

There is a tremendous difference between results. LEM flame speed is much smaller than G-equation turbulent flame speed. As demonstrated in section 6.2, the G-equation turbulent flame speed used in this study is not well suited in the lean conditions, and the increase in flame speed due to turbulence is over-predicted. It is computed that the LEM resolution is not fine enough to capture all the turbulence scales. As a consequence, the local flame speed may be under-predicted: turbulence-enhanced combustion is not fully resolved, or the local flame speed may be over-predicted: the flame front fails to quench. Nevertheless, one expect the LEM results to be a better representation of the actual flame shape when compared to the G-LES approach since turbulent flame speed model is not valid in the broken reaction zone.

7.2 Computational Cost

The G-equation approach tracks only one variable (G) in a perfectly premixed system and three (G,Z and Z''^2 in a partially premixed system. The derivation of the G-equation reaction rate has a negligible computational cost. In the LEM methodology, the Lagrangian tracking of species, temperature, density and energy has a limited cost but the computation of the chemical reaction rate can be tremendous. Nevertheless a strategy for efficient chemistry computation (Neural Network[28]) can greatly improve the computation speed. In Table 7, the computational cost difference between G-equation and LEM with direct integration of the chemical reaction rates are reported.

Combustion Model		Cost
G-Equation	- No reaction	1.0
LEM (12 cells)	- No reaction	1.1
LEM (12 cells)	- Direct Integration	7.0

Table 7 Relative computational cost for different methodologies.

The cost of direct integration being prohibitive, methods like ISAT or ANN have to be implemented. Past studies[10] have shown that ISAT can speed up the chemistry by a factor of 30 to 50. However, in transient simulations like LES, the ISAT table will continue to grow even after statistically stationary state is reached and can overwhelm the processor memory.

An alternative method based on ANN[29] has been developed. The Neural Network is trained on the a priori accessible composition space and then implemented within the chemistry solver. ISAT and ANN both have to potential ability to drastically reduce the CPU cost of carrying out finite-rate kinetics and their implementation within the LES-LEM is an ongoing effort.

7.3 Emissions

Even though the flame length is much longer when LEM is used, the same emission prediction where obtained (for both CO and NO). This confirms that the CO formed at the flame front has no effect upon CO mass fraction at the location of the emission probe. Therefore, CO prediction strongly depends upon UHC formation and oxidation. Emission prediction with LEM are shown in Figs. 8 and 9.

8 Conclusion

The G-equation approach is shown to be a very poor model to simulate the behavior of very lean combustion system (invalid flame speed model, no quenching and re-ignition capability). On the other hand, LEM represents a very powerful tool to study such systems. Use of Artificial Neural Network to compute the chemical reaction rates may ensure a fast computation of the chemistry parameters, thus making LES+LEM a promising technique to study pollutant emission near LBO.

Emission predictions are in good agreement with experimental data. Nevertheless, the use of a flame quenching model and the uncertainty in the UHC oxidation rate does not allow accurate predictions. It is shown that flame quenching and re-ignition of unburnt reactant must be simulated. LES+LEM appears to be a powerful technique to handle this challenge but will

require proper kinetics model implemented as an efficient scheme.

Acknowledgments

This work was made possible with the support in part by General Electric Aircraft Engine Company and CFD Research Corporation, AL (prime sponsors are Department of Energy and Wright Patterson AFB). Support for some of the computations was provided by DOD HPC Center at ERDC (MS).

References

[1] Bhargava, A., Kendrick, D. W., Colket, M. B., Sowa, W. A., Casleton, K. H., and Maloney, D. J., "Pressure Effects on NO_x and CO emission in industrial gas turbines," *Trans. of the ASME*, Vol. 2000-GT-8, 2000.

[2] Erlebacher, G., Hussaini, M. Y., Speziale, C. G., and Zang, T. A., "Toward the Large-Eddy Simulation of Compressible Turbulent Flows," *Journal of Fluid Mechanics*, Vol. 238, 1992, pp. 155–185.

[3] Kim, W.-W., Menon, S., and Mongia, H. C., "Large-Eddy Simulation of a Gas Turbine Combustor Flow," *Combustion Science and Technology*, Vol. 143, 1999, pp. 25–62.

[4] Held, T. J., Mueller, M. A., and Mongia, H. C., "A Data-Driven Model for NO_x, CO and UHC Emissions for a Dry Low Emissions Gas Turbine Combustor," *AIAA-2001-3425*, 2001.

[5] Stone, C. and Menon, S., "Numerical Simulation of Combustion Dynamics in a Swirling Dump Combustor," *Proceedings of Grand Challenges In Computer Simulations, High Performance Computing 2001*, SCS Press, 2001, pp. 15–20.

[6] Peters, N., *Turbulent Combustion*, Cambridge Monographs on Mechanics, 2000.

[7] Pocheau, A., "Scale Invariance in Turbulent Flont Propagation," *Physical Review E*, Vol. 49, 1994, pp. 1109–1122.

[8] Chen, J.-Y., Private Communication.

[9] Pope, S., "Computationally Efficient implementation of combustion chemistry using in situ adaptive tabulation," *Combustion Theory Modelling*, Vol. 1, 1997, pp. 41–63.

[10] Sankaran, V. and Menon, S., "The Structure of Premixed Flame in the Thin-Reaction-Zones Regime," *Proceedings of the Combustion Institute*, Vol. 28 (to appear), 2000.

[11] Haykin, S., "Neural Networks: A Comprehensive foundation," *Neural Networks: A Comprehensive foundation*, Prentice Hall, Hamilton, Ontario, Canada, 1999, pp. 2–2.

[12] Beale, M. and Demuth, H., "Neural Network Toolbox," *Neural Network Toolbox*, The Math Works, Inc., Natick, MA, 1998, p. 5.25.

[13] Held, T. J. and Mongia, H. C., "Emissions Modeling of Gas Turbine Combustors using a Partially-premixed Laminar Flamelet Model," *AIAA-98-3950*, 1998.

[14] Eggenspieler, G. and Menon, S., "LES of Premixed Combustion and Pollutant Emission in a DOE-HAT Combustor," *AIAA-2003-0309*, 2003.

[15] Westbrook, C. K. and Dryer, F. L., "Simplified Reaction Mechanisms for the Oxidation of Hydrocarbon Fuels in Flames," *Combustion Science and Technology*, Vol. 27, 1981, pp. 31–43.

[16] Turns, S. R., *An Introduction to Combustion. Concept and Applications*, Mac Graw Hill, 1999.

[17] Meneveau, C. and Poinsot, T., "Stretching and Quenching of Flamelets in Premixed Turbulent Combustion," *Combustion and Flame*, Vol. 86, 1991, pp. 311–332.

[18] Poinsot, T., Veynante, D., and Candel, S., "Quenching processes and premixed turbulent combustion diagrams," *Journal of Fluid Mechanics*, Vol. 228, 1991, pp. 561–606.

[19] Cannon, S. M., Zuo, B., and Smith, C. E., "LES Predictions of Combustor Emissions From a Practical Industrial Fuel Injector," *ASME-2000-GT-98*, 2003.

[20] Fric, T. F., "Effects of Fuel-Air Unmixedness on NOx Emissions," *Journal of Propulsion and Power*, Vol. 9, No. 5, 1993, pp. 708–713.

[21] Peters, N., "The turbulent Burning Velocity for Large-scale and small scale turbulence," *Journal of Fluid mechanics*, Vol. 384, 1999, pp. 107–132.

[22] Borghi, R., "On the Structure and Morphology of Turbulent Premixed Flames," *Recent Advances in Aerospace Sciences*, edited by C. Casci and C. Bruno, Plenum Press, 1985, pp. 117–138.

[23] Pitsch, H. and Duchamp De Lageneste, L., "Large-Eddy Simulation of Premixed Turbulent Combustion Using a Level-Set Approach," *Twenty-Ninth Symposium (International) on Combustion*, 2002, pp. 2001–2008.

[24] Chakravarthy, V. and Menon, S., "Large-Eddy Simulations of Turbulent Premixed Flames in the Flamelet Regime," *Combustion Science and Technology*, Vol. 162, 2000, pp. 1–48.

[25] Kim, W.-W. and Menon, S., "Numerical Simulations of Turbulent Premixed Flames in the Thin-Reaction-Zones Regime," *Combustion Science and Technology*, Vol. 160, 2000, pp. 119–150.

[26] Duclos, J. M., Veynante, D., and Poinsot, T., "A Comparison of Flamelet Models for Premixed Turbulent Combustion," *Combustion and Flame*, Vol. 95, 1993, pp. 101–117.

[27] Smith, T. and Menon, S., "One-dimensional simulations of freely propagating turbulent premixed flames," *Combustion Science and Technology*, Vol. 128, 1996, pp. 99–130.

[28] Kapoor, R., Lentati, A., and Menon, S., "Simulations of methane-air flames using ISAT and ANN," *AIAA-2001-3847*, 2001.

[29] Menon, S., "The Use and Relevance of Reacting LES on Engineering Design Cycle," *Direct and Large Eddy Simulation IV*, 2001, pp. 509–516.

[30] Bédat, B. and Cheng, R. K., "Experimental Study of Premixed Flames in Intense Isotropic Turbulence," *Combustion and Flame*, Vol. 100, 1995, pp. 486–494.

[31] Mansour, M., Peters, N., and Chen, Y., "Investigation of Scalar Mixing in the Thin Reaction Zones Regime using a simultaneous CH-LIF/Rayleigh Laser Technique," *Twenty-Seventh Symposium (International) on Combustion*, 1998, pp. 767–773.

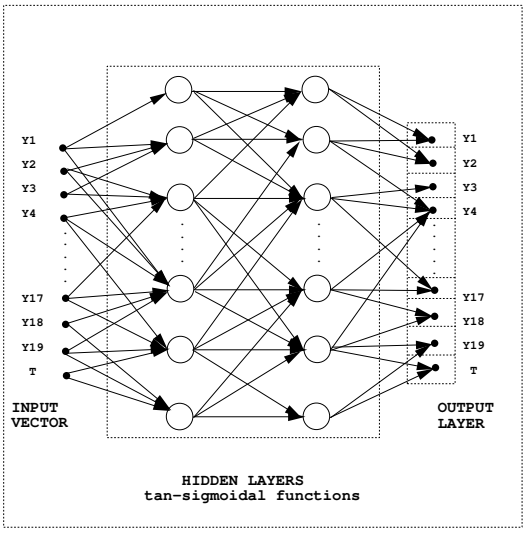

Figure 1 A three-layer neural network structure

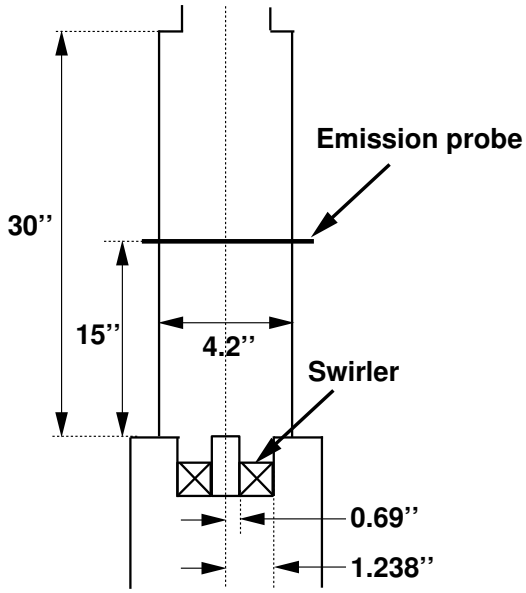

a) Sketch of the DOE-HAT Combustor setup

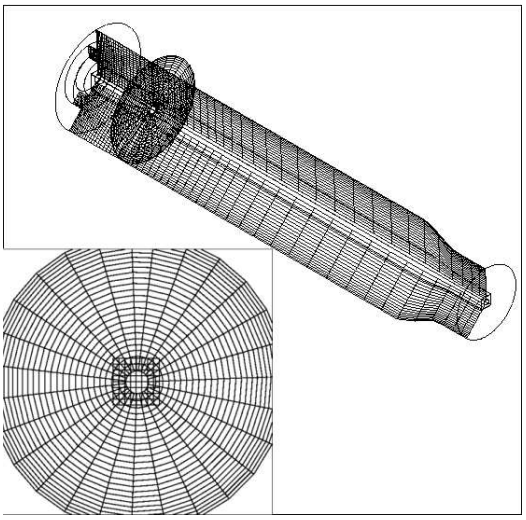

b) General view of the 3D computational domain

Figure 2 Geometry and dimensions of the DOE-HAT combustor and the computational domain. View of the centerline cartesian grid overlapping the cartesian grid (Bottom left hand side corner of Fig. b)

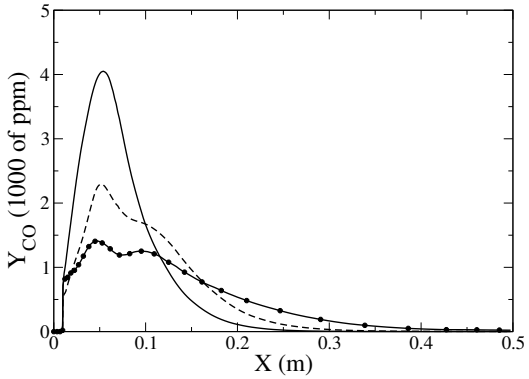

Figure 3 Influence of the flame speed model upon the CO mass fraction. X is the distance from the combustion chamber dump plane. (— : β=20.0, ζ = 16.56, - - : β=10.0, ζ = 10.00, -•- : β=7.0, ζ = 10.00)

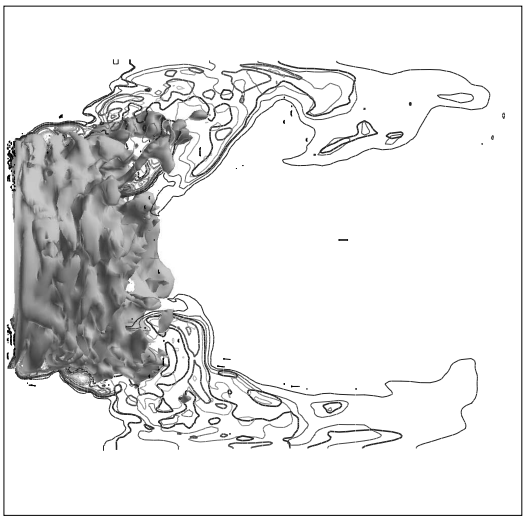

Figure 4 Instantaneous snapshot of the flame surface, Y_{UHC} isolines (thick contours) and Y_{CO} isolines (thin contours).

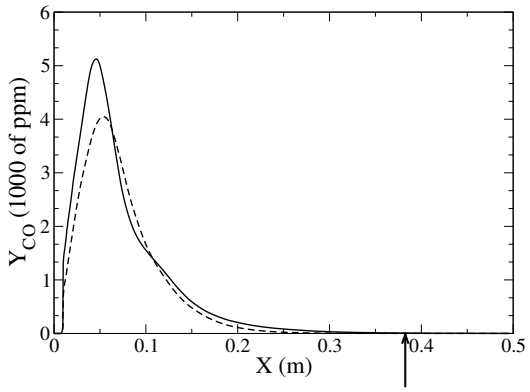

Figure 5 Time-averaged CO mass fraction as a function of the distance from the dump plane (— : CO production via UHC oxidation is taken into account, - - : CO production via UHC oxidation is not taken into account). The location of the emission probe is indicated by an arrow.

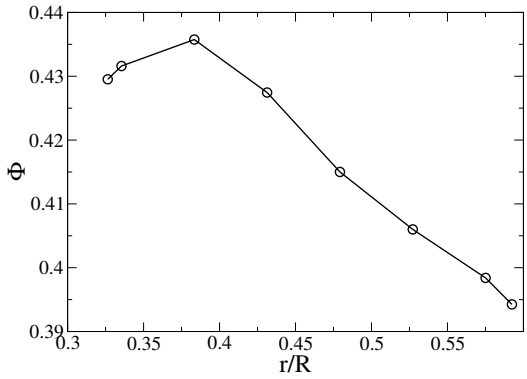

a) Inflow Φ as a function of the normalized radius ($\overline{\Phi}$=0.415) - Courtesy: UTRC

b) Time averaged mixture fraction field. Dark colors: leaner than $\overline{\Phi}$, light colors: richer than $\overline{\Phi}$

Figure 7 Unmixindness of the inflow mixture. Inflow profile and time averaged $\widetilde{Z}$ field

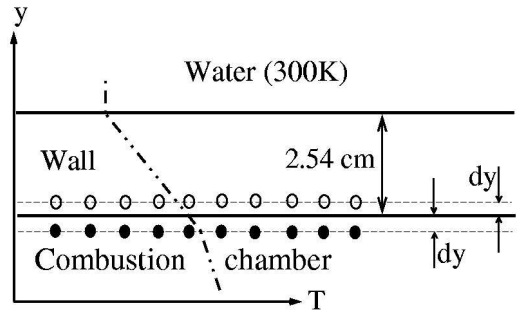

Figure 6 Sketch of the geometry of the combustion chamber walls to take into account the heat losses related to the water cooling system. •: computed LES grid points, ∘: boundary grid points.

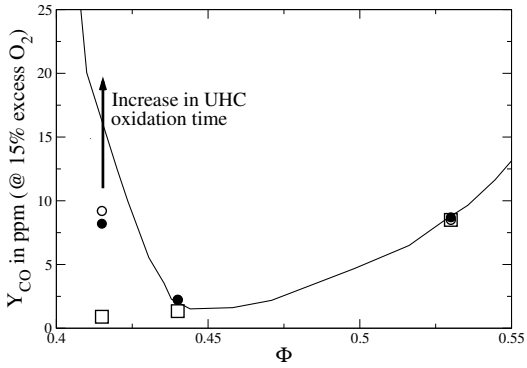

Figure 8 Experimental and numerical CO emission for different equivalence ratio (— Experiments, •: LES - LEM, □: LES - G-equation with no model for UHC, ∘: LES - G-equation).

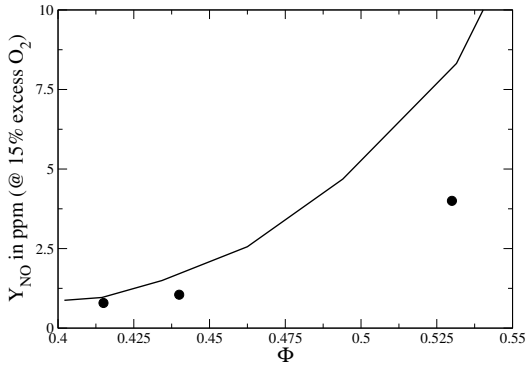

Figure 9 Experimental and numerical *NO* emission for different equivalence ratio(— Experiments, •: LES - LEM as well as LES - G-equation).

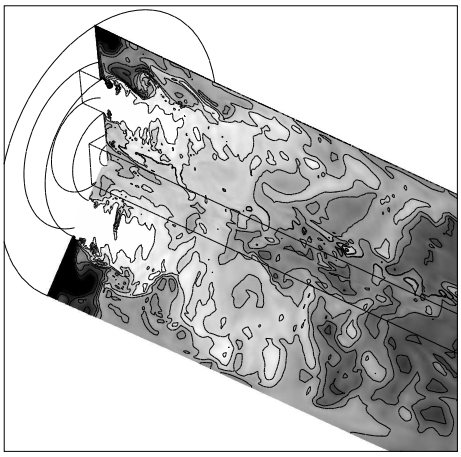

a) Φ=0.53. Light gray = 4 ppm, Dark gray = 11 ppm

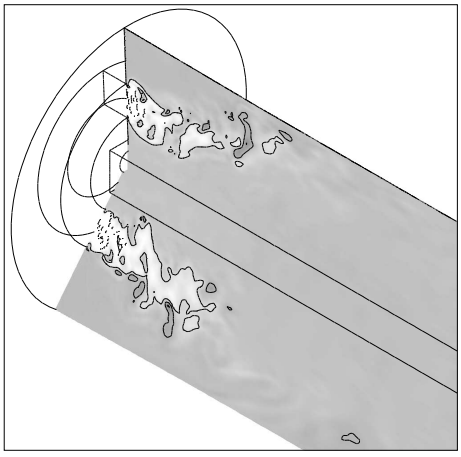

b) Φ=0.41. Light gray = 0 ppm, Dark gray = 6 ppm

Figure 10 Instantaneous *NO* mass fraction field. Large amount of *NO* are produced via Zeldovitch mechanism for Φ=0.53 while the entire amount of *NO* is produced at the flame front for Φ=0.41

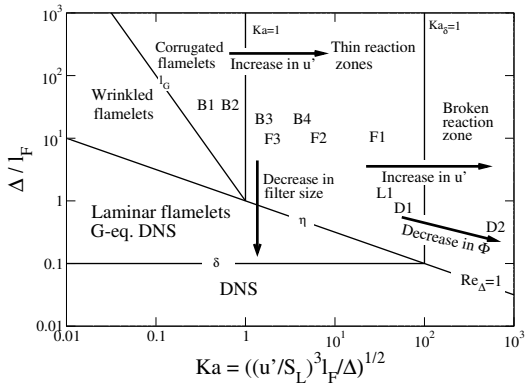

Figure 11 Combustion regimes for LES of turbulent premixed combustion. B-type[30] and F-type[31] flames are located as well as the LM-6000 gas turbine[3] (designated by L1) and the current gas turbine (designated by D1 for Φ>0.5 and by D2 for Φ<0.5)

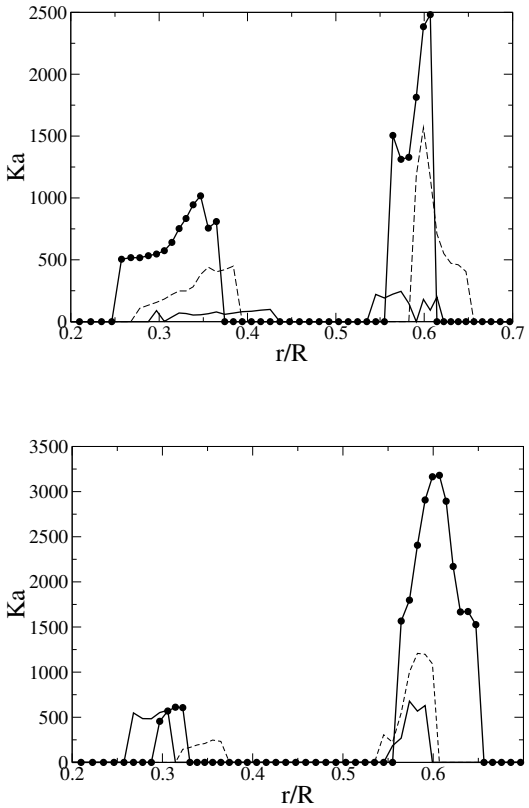

b) LES / LEM

Figure 12 Local instantaneous Flame front Karlovitz number for different equivalence ratio. Data were taken at 1 cm from the dump plane in a plane parallel to the dump plane (–: Φ=0.53, - -: Φ=0.44, -•-: Φ=0.41).